Lower edge of locked Main Himalayan Thrust unzipped by the 2015 Gorkha earthquake

Jean-Philippe Avouac[1], Lingsen Meng[2], Shengji Wei[3], Teng Wang[4], Jean-Paul Ampuero[5]

[1] Department of Earth Sciences, University of Cambridge, UK
[2] Department of Earth, Planetary and Space Sciences, University of California, Los Angeles, CA, USA
[3] Earth Observatory of Singapore, Nanyang Technological University, Singapore
[4] Huffington Department of Earth Sciences, Southern Methodist University, Dallas, TX, USA
[5] Seismological Laboratory, California Institute of Technology, Pasadena, CA, USA

Large earthquakes are thought to release strain on previously locked faults. However, the details of how earthquakes are initiated, grow and terminate in relation to pre-seismically locked and creeping patches is unclear[1-4]. The 2015 Mw 7.8 Gorkha, Nepal earthquake occurred close to Kathmandu in a region where the prior pattern of fault locking is well documented[5]. Here we analyze this event using seismological records measured at teleseismic distances and Synthetic Aperture Radar imagery. We show that the earthquake originated northwest of Kathmandu within a cluster of background seismicity that fringes the bottom of the locked portion of the Main Himalayan Thrust fault (MHT). The rupture propagated eastwards for about 140 km, unzipping the lower edge of the locked portion of the fault. High-frequency seismic waves radiated continuously as the slip pulse propagated at about 2.8 km s-1 along this zone of presumably high and heterogeneous pre-seismic stress at the seismic-aseismic transition. Eastward unzipping of the fault resumed during the Mw 7.3 aftershock on May 12. The transfer of stress to neighbouring regions during the Gorkha earthquake should facilitate future rupture of the areas of the MHT adjacent and up-dip of the Gorkha earthquake rupture.

On April 25 2015, a destructive Mw 7.8 earthquake occurred along the Himalayan front close to Kathmandu (Figure 1). The epicenter was located 80 km to the west-northwest of Kathmandu within a long-identified zone of clustered seismicity which runs beneath the front of the high Himalaya[6]. The focal mechanism[7] indicating thrusting on a subhorizontal fault dipping about 10° and the 15 km hypocentral depth[7] make it likely that this earthquake ruptured the MHT, the main fault along which northern India underthrusts the Himalaya at a rate of approximately 2 cm/yr[8]. A Mw7.3 aftershock with a very similar focal mechanism[7] occurred on May 12, 75km east of Kathmandu (Figure 1). The geometry of the MHT in the hypocentral area is relatively well known from various geophysical experiments[9,10]. Geodetic measurements collected over the last 20 years revealed that this fault remained locked over this time period[5,11] and the pattern of locking is now well constrained[5] (Figure 1), allowing for a detailed comparison with the rupture process during the Gorkha earthquake.

We imaged the rupture process by back-projecting[12] teleseismic P waves recorded by the Australian seismic network (Figures 2a and S1) using the Multitaper-MUSIC array processing technique. The technique tracks the spatio-temporal evolution of the sources of high frequency radiation (0.5-2 Hz) during the rupture process (Figure S2; see Methods). The back-projection forms coherent sources for about 60s after initiation of the rupture. The high frequency sources are almost linearly distributed for about 45s and their timing indicates a 2.72+/-0.13 km/s eastward propagation (Figure 2b). They follow remarkably well the downdip edge of the locked zone (Figure 1) and the cluster of background seismicity (Figure 2a) including a local kink northwest of Kathmandu. The amplitude rises sharply from 10 to 20s, peaks from 20 to 40s and decays abruptly after about 45s (Figure 2c). High frequency radiation persists after 45s but migrates updip in a southeastward direction. The May 12 aftershock occurred a few tens of kilometers east of where the initial phase of along strike propagation of the rupture stopped (Figure 2a).

We also determined a finite source model of the rupture from the joint inversion[13] of teleseismic waveforms in the 0.01-1 Hz frequency band and static surface displacements measured from SAR image offsets. The fault is assumed planar and its dip angle was adjusted to 7° by trial and. The model assumes that, once initiated, slip accrues over a certain duration (rise time) in the wake of the rupture front. The inversion solves for the final slip amplitude, rake, rise-time and rupture front velocity at each grid point (see Methods). The source model is determined so as to best fit the static surface displacements (Figure S3) and teleseismic waveforms (Figure S4). The static surface displacements were measured using European Space Agency's Sentinel-1 radar images acquired on 17^{th} and 29^{th} of April, and 9^{th} April and 3^{rd} May. We ignored the possibility of postseismic deformation over the 4 and 8 days following the event (see Methods). The finite-source model (Figure 2) shows that the rupture propagated eastward at 3.0+/- 0.5 km/s on average (Figure S5). The slip area is about 120 km in length along strike and 50km in width along dip. The implied moment tensor is nearly identical to the W-phase moment tensor (Figure 1). Altogether the earthquake released a total moment of 7.2×10^{20} N.m, corresponding to a moment magnitude Mw 7.84. The moment rate function shows a simple rupture with a single major pulse of 50s duration (Figure 2c). The May 12 aftershocks falls in a gap of relatively low slip at the eastward termination of the mainshock.

The results from the back-projection and finite source inversion are in remarkable agreement during the first 45s of the rupture. The moment release rate and the power of the high frequency sources show the same temporal pattern (Figure 2c). Both source imaging techniques reveal a unilateral pulse-like rupture with a narrow strip of active slip, 20-30 km wide along strike, propagating eastwards at about 2.7 to 3.0 km/s (Figure 3 and Supplementary Animation). Contrary to the backprojection, the finite source model yields a rupture velocity which is sensitive to the epicentral location, which can be off by more than 10km. Given the various possible sources of errors, we estimate that the two analysis agree within uncertainties and indicate a rupture velocity of 2.8+/-0.3 km/s.

Because the finite-source inversion assumes a rupture front expanding from the epicenter and because the teleseismic waveforms only constrain robustly the moment rate function, the slip distribution for each time interval is smeared along the quasi-circular isochrons of the rupture front (Figure 3). The SAR data help limit this smearing effect by forcing the cumulative slip distribution to match the west-east trending narrow zone of surface deformation along the rupture-propagation pathway (Figure S3). The northern edge of the high slip area correlates with the location of the high frequency sources and with the edge of the locked zone (Figure 2a). After 45s the source model is less well constrained because of the lower signal-to-noise ratio and the pulse becomes more diffuse and smeared along isochrons.

Both the back-projection results and the finite-fault source model suggest that the earthquake unzipped the downdip edge of the locked zone, propagating mostly as a mode-III crack. The persistent radiation of high frequency waves along the whole rupture length is probably due to the high and heterogeneous stresses built up at the transition between the locked and the creeping zone. The stress heterogeneities can result from intermingling of creeping and locked areas at a scale not resolvable with surface geodesy. Another factor contributing to stress heterogeneity is the background seismicity, which is well understood to be triggered by stress build-up at the downdip edge of the locked zone[5,14]. The correlation between the moment rate and the power of high frequency seismic radiations suggests that the high frequency sources are "riding the wave" of an ongoing slip pulse. It is interesting to note that, although tremors-and-slip events are note directly comparable to standard earthquakes, a similar correlation has been observed during tectonic tremor episodes on subduction megathrust[15]. The Gorkha earthquake actually shares similarities with earthquakes observed near the downdip end of the locked subduction megathrust[1] (zone C of Lay et al.[16]). In both settings, the high frequency sources are found to radiate from the lower edge of the locked fault zone.

The rupture during the Gorkha earthquake expanded upwards from the locked edge, but not much downwards probably because the zone of aseismic slip acted as an efficient barrier[4] to downdip propagation of the seismic rupture or because of the restraining effect of a ramp along the MHT[6]. The pattern of coupling can thus explain the location of the earthquake initiation and the rupture process but not its arrest along strike.

The rupture seems to have derailed from its linear along-strike propagation after ~45s close to the location of the May 12 Mw 7.3 aftershock, although the trend toward the Australian network suggest that it could reflect a ‘swimming’ artifact (mitigation of this artifact by the MUSIC technique is imperfect when the energy gets weak). In any case, the eastward rupture propagation was possibly arrested when it encountered some structural complexity, a zone of lower stress on the MHT due to past seismicity or a rate strengthening patch, which could have inhibited the rupture propagation. Interestingly, the mainshock and the May 12 aftershock ruptured nearly entirely a segment of persistently intense background seismicity over the last 20 years of local seismic monitoring. The rupture initiated clearly at the western end of this segment. Lateral variations of the background seismicity and of the pattern and intensity of high frequency sources could reflect lateral ramps along the MHT[17].

The 2015 Gorkha earthquake is similar in location to the 1833 earthquake, with estimated magnitude Mw 7.6-7.7, which also caused heavy damages in Kathmandu[18,19]. These earthquakes clearly did not propagate to the front of the Himalaya where the MHT emerges at the surface. Paleoseismological studies have shown that several larger Himalayan earthquakes did however reach the surface[20,21]. In particular, the 1934 Bihar-Nepal earthquake[22] ruptured the MHT east of Kathmandu (Figure 1) producing over 6 m of slip at the surface and reaching an estimated magnitude of Mw 8.2[23]. Its rupture extent is weakly constrained but consistent with the possibility that the Gorkha earthquake sequence arrested because of the lower stress level left by the 1934 event or due to some local complexity of structural origin. A lateral ramp of the MHT, or an heterogeneity of fault friction, for example a small patch with rate-strengthening friction not resolvable with the interseismic geodetic data, could have resulted in a barrier effect and a persistent segmentation of the MHT.

A previous large earthquake in 1255 also reached the surface[22,23]. The area east of Kathmandu seems unlikely to rupture again in the near future in a large (say Mw>7.5) event. The 81 yr time span since 1934 is short in comparison to the 679 yr separation between 1255 and 1934; the acumulated slip deficit since 1934 amounts to less than 2 m. The 1813 and 2015 earthquakes must have contributed to the process of upward transfer of the stresses which build up around the downdip edge of the locked fault zone in the interseismic period. This mechanism is observed in dynamic models of the seismic cyle and ultimately leads to rupture of the whole locked zone[24]. It is also possible that the 2015 and 1833 earthquakes produced similar ruptures and failed to rupture the locked portions of the MHT beneath and west of the Kathmandu basin because of some persistent barrier of mechanical or structural origin. Yet another possibility is that slip on the updip locked portion of the MHT is not entirely seismic. The stress increase could in principle be released by afterslip if the updip fault portion obeyed a rate-strengthening friction law and were previously lying in the stress shadow[25] of the asperity which ruptured in 2015. If so, it should be observed to slip aseismically in the postseismic period.

The locked portion of the MHT west of the 2015 event calls for special attention as the nearly 800 km long stretch between the 1833/2015 ruptures and the 1905 Mw 7.8 Kangra earthquake is a well identified seismic gap with no large earthquake for over 500 years [17,21,26]. The MHT is clearly locked there (Figure 1) and its deficit of slip could exceed 10 m. The last large earthquake there occurred in 1505, and could have exceeded Mw 8.5[27] . This event produced significant damage in southern Tibet and ruptured the Himalayan foothills at the surface[28]. While the size of that particular event is debated, there is general consensus that major earthquakes (Mw>8.5) occurred along that stretch of the Himalaya, and could have produced over 10 m of slip along the Himalayan front[17,21,26].

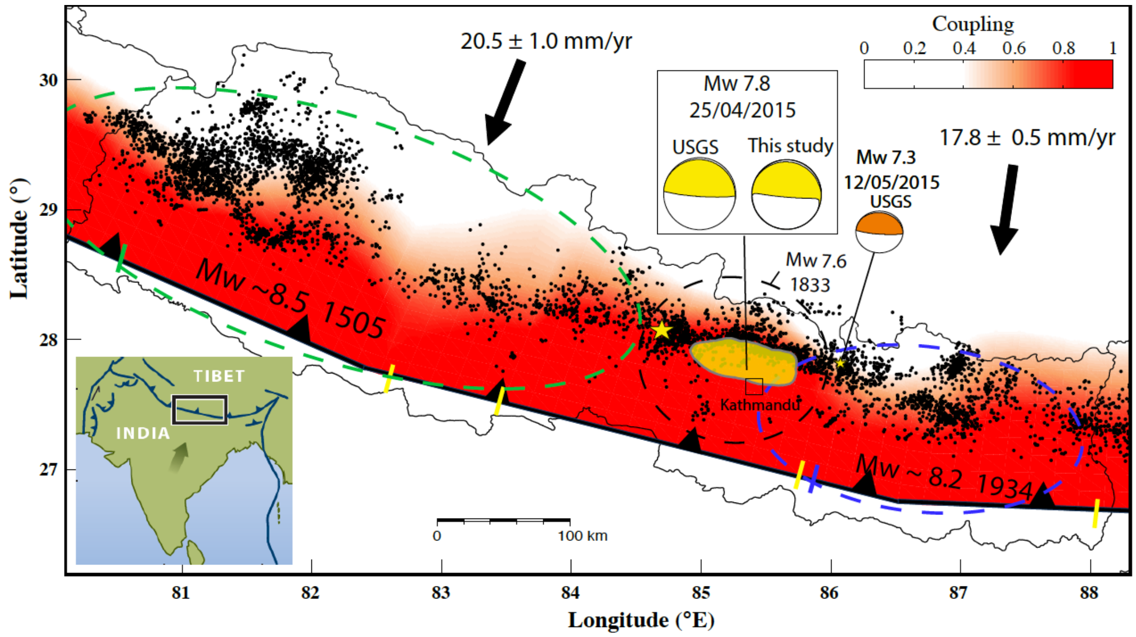

Figure 1: Seismotectonic context of the 2015 Mw 7.8 Gorkha earthquake. Yellow patch shows area with >1m coseismic slip. Epicenter (star), centroid location and W-phase moment tensor from USGS[7]. Interseismic coupling and convergence rate across the Himalaya from Ader et al.[5]. Dots show 1995-2003 relocated seismicity[29]. Mw>7.5 historical events since 1505 [17-19,22] are estimated to have occurred within the ellipses. Blue and green short lines show locations of documented surface rupture in 1934 and 1505 respectively[23,28]. Yellow short lines indicate surface ruptures more probably related to older events (possibly in 1255 AD)[17,23]. Inset: map location and motion of India relative to Eurasia.

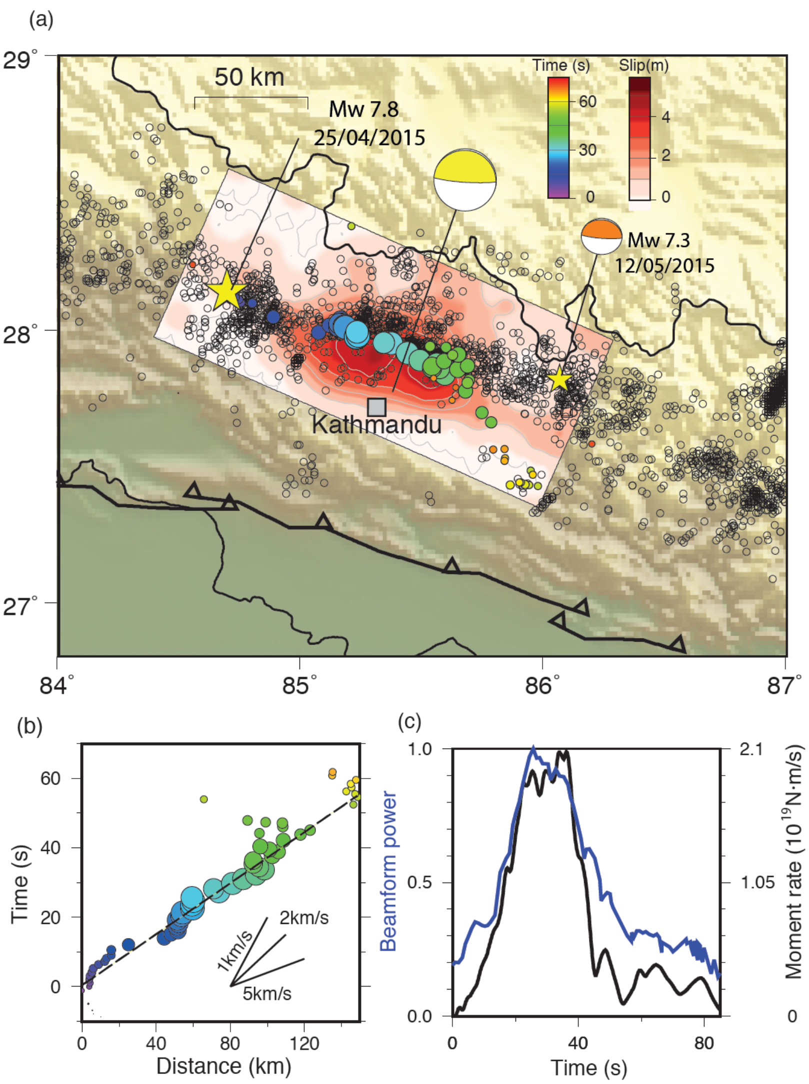

Figure 2: Seismic rupture kinematics. (a) Co-seismic slip determined from joint inversion of teleseismic waveforms and SAR measurements (red shading) and locations of high frequency (0.5-2 Hz) sources determined from backprojection of teleseismic waves (dots). Size is proportional to beamforming amplitude and color indicates time of each window center relative to hypocentral time. Open circles show relocated background 1995-2003 seismicity[29]. (b) Timing of high frequency sources as a function of distance along strike. Least squares linear regression (dashed line) indicates a rupture speed of 2.72+/-0.13 km/s. (c) Relative beamforming power (blue) and moment release rate from finite source inversion (black).

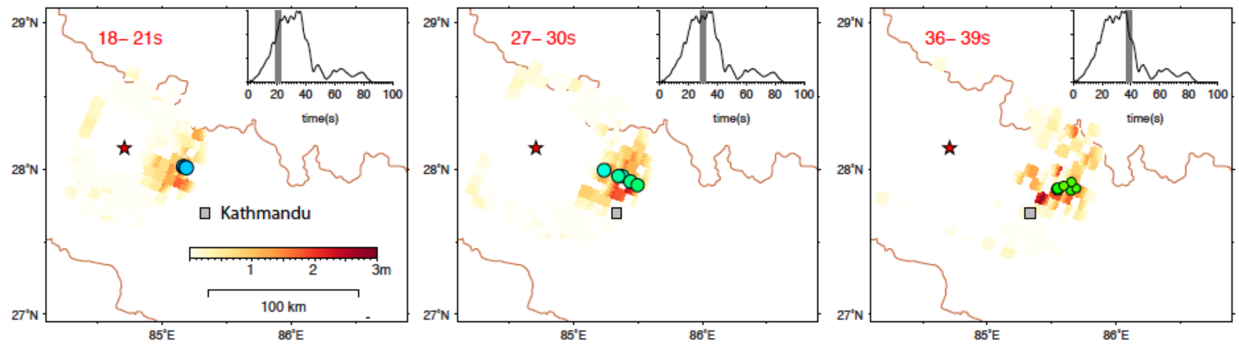

Figure 3: Time snapshots of seismic rupture evolution. Each plot shows slip (background colors) and high-frequency sources (dots, colored by their rupture time, same scale as in Figure 2) occurring within a 3s window indicated by a grey band over the source time function in the inset. An animation is provided as supplementary material.

References

1 Schurr, B. *et al.* Gradual unlocking of plate boundary controlled initiation of the 2014 Iquique earthquake. *Nature* **512**, 299-302, doi:10.1038/nature13681 (2014).

2 Loveless, J. P. & Meade, B. J. Spatial correlation of interseismic coupling and coseismic rupture extent of the 2011 M-W=9.0 Tohoku-oki earthquake. *Geophysical Research Letters* **38**, doi:10.1029/2011gl048561 (2011).

3 Yue, H. *et al.* The 5 September 2012 Nicoya, Costa Rica M-w 7.6 earthquake rupture process from joint inversion of high-rate GPS, strong-motion, and teleseismic P wave data and its relationship to adjacent plate boundary interface properties. *Journal of Geophysical Research-Solid Earth* **118**, 5453-5466, doi:10.1002/jgrb.50379 (2013).

4 Kaneko, Y., Avouac, J. P. & Lapusta, N. Towards inferring earthquake patterns from geodetic observations of interseismic coupling. *Nature Geoscience* **3**, 363-U324, doi:10.1038/ngeo843 (2010).

5 Ader, T. *et al.* Convergence rate across the Nepal Himalaya and interseismic coupling on the Main Himalayan Thrust: Implications for seismic hazard. *Journal of Geophysical Research-Solid Earth* **117**, doi:10.1029/2011jb009071 (2012).

6 Pandey, M. R., Tandukar, R. P., Avouac, J. P., Lave, J. & Massot, J. P. Interseismic Strain Accumulation on the Himalaya Crustal Ramp (Nepal). *Geophysical Research Letters* **22**, 751-754 (1995).

7 USGS. *The 2015 Gorkha earthquake* http://earthquake.usgs.gov/earthquakes/eventpage/us20002926 *and its Mw 7.3 aftershock* http://earthquake.usgs.gov/earthquakes/eventpage/us20002ejl - general_summary, 2015).

8 Lavé, J. & Avouac, J. P. Active folding of fluvial terraces across the Siwaliks Hills, Himalayas of central Nepal. *Journal of Geophysical Research-Solid Earth* **105**, 5735-5770 (2000).

9 Nabelek, J. *et al.* Underplating in the Himalaya-Tibet Collision Zone Revealed by the Hi-CLIMB Experiment. *Science* **325**, 1371-1374, doi:10.1126/science.1167719 (2009).

10 Lemonnier, C. *et al.* Electrical structure of the Himalaya of Central Nepal: high conductivity around the mid-crustal ramp along the MHT. *Geophysical Research Letters* **26**, 3261-3264 (1999).

11 Bilham, R. *et al.* GPS measurements of present-day convergence across the Nepal Himalaya. *Nature* **386**, 61-64 (1997).

12 Ishii, M., Shearer, P. M., Houston, H. & Vidale, J. E. Extent, duration and speed of the 2004 Sumatra-Andaman earthquake imaged by the Hi-Net array. *Nature* **435**, 933-936 (2005).

13 Ji, C., Wald, D. & Helmberger, D. V. Source Description of the 1999 Hector Mine, California Earthquake, Part I: Wavelet Domain Inversion Theory and Resolution Analysis. *Bulletin of the Seismological Society of America* **92**, 1192-1207 (2002).

14 Cattin, R. & Avouac, J. P. Modeling mountain building and the seismic cycle in the Himalaya of Nepal. *Journal of Geophysical Research-Solid Earth* **105**, 13389-13407 (2000).

15 Ide, S., Imanishi, K., Yoshida, Y., Beroza, G. C. & Shelly, D. R. Bridging the gap between seismically and geodetically detected slow earthquakes. *Geophysical Research Letters* **35**, doi:10.1029/2008gl034014 (2008).

16 Lay, T. *et al.* Depth-varying rupture properties of subduction zone megathrust faults. *Journal of Geophysical Research-Solid Earth* **117**, doi:10.1029/2011jb009133 (2012).

17 Mugnier, J. L. *et al.* Structural interpretation of the great earthquakes of the last millennium in the central Himalaya. *Earth-Science Reviews* **127**, 30-47, doi:10.1016/j.earscirev.2013.09.003 (2013).

18 Ambraseys, N. N. & Douglas, J. Magnitude calibration of north Indian earthquakes. *Geophysical Journal International* **159**, 165-206 (2004).

19 Bilham, R. Location and Magnitude of the 1833 Nepal Earthquake and Its Relation to the Rupture Zones of Contiguous Great Himalayan Earthquakes. *Current Science* **69**, 101-128 (1995).

20 Lavé, J. *et al.* Evidence for a great medieval earthquake (approximate to 1100 AD) in the Central Himalayas, Nepal. *Science* **307**, 1302-1305 (2005).

21 Kumar, S. *et al.* Paleoseismic evidence of great surface-rupture earthquakes along the Indian Himalaya. *Journal of Geophysical Research-Solid Earth* **111**, doi: 10.1029/2004JB003309 (2006).

22 Sapkota, S. N. *et al.* Primary surface ruptures of the great Himalayan earthquakes in 1934 and 1255. *Nature Geoscience* **6**, 71-76, doi:10.1038/ngeo1669 (2013).

23 Bollinger, L. *et al.* Estimating the return times of great Himalayan earthquakes in eastern Nepal: Evidence from the Patu and Bardibas strands of the Main Frontal Thrust. *Journal of Geophysical Research-Solid Earth* **119**, 7123-7163, doi:10.1002/2014jb010970 (2014).

24 Lapusta, N., Rice, J. R., Ben-Zion, Y. & Zheng, G. T. Elastodynamic analysis for slow tectonic loading with spontaneous rupture episodes on faults with rate- and state-

dependent friction. *Journal of Geophysical Research-Solid Earth* **105**, 23765-23789 (2000).

25 Burgmann, R. *et al.* Interseismic coupling and asperity distribution along the Kamchatka subduction zone. *Journal of Geophysical Research-Solid Earth* **110** (2005).

26 Rajendran, C. P., John, B. & Rajendran, K. Medieval pulse of great earthquakes in the central Himalaya: Viewing past activities on the frontal thrust. *Journal of Geophysical Research-Solid Earth* **120**, 1623-1641, doi:10.1002/2014jb011015 (2015).

27 Bilham, R. & Wallace, K. Future Mw>8 earthquakes in the Himalaya: implications from the 26 Dec 2004 Mw=9.0 earthquake on India's eastern plate margin. *Geol. Surv. India Spl. Pub* **85**, 1-14 (2005).

28 Yule, D., S. Dawson, J. Lave, S. Sapkota, and D. Tiwari. in *AGU Fall Meeting.*

29 Rajaure, S., S. N. Sapkota, L. B. Adhikari, B. Koirala, M. Bhattarai, D. R. Tiwari, U. Gautam, P. Shrestha, S. Maske, J. P. Avouac, L. Bollinger and M. R. Pandey. Double difference relocation of local earthquakes in the Nepal Himalaya. *Journal of Nepal Geological Society*, 133-142 (2013).

30 Vandecar, J. C. & Crosson, R. S. Determination of teleseismic relative phase arrival times using multi-channel cross-correlation and least-squares. *Bulletin of the Seismological Society of America* **80**, 150-169 (1990).

31 Meng, L. S., Inbal, A. & Ampuero, J. P. A window into the complexity of the dynamic rupture of the 2011 Mw 9 Tohoku-Oki earthquake. *Geophysical Research Letters* **38**, doi:10.1029/2011gl048118 (2011).

32 Meng, L., Ampuero, J. P., Sladen, A. & Rendon, H. High-resolution backprojection at regional distance: Application to the Haiti M7.0 earthquake and comparisons with finite source studies. *Journal of Geophysical Research-Solid Earth* **117**, doi:10.1029/2011jb008702 (2012).

33 Meng, L. S., Ampuero, J. P., Luo, Y. D., Wu, W. B. & Ni, S. D. Mitigating artifacts in back-projection source imaging with implications for frequency-dependent properties of the Tohoku-Oki earthquake. *Earth Planets and Space* **64**, 1101-1109, doi:10.5047/eps.2012.05.010 (2012).

34 De Zan, F. & Guarnieri, A. M. TOPSAR: Terrain observation by progressive scans. *IEEE Transactions on Geoscience and Remote Sensing* **44**, 2352-2360, doi:10.1109/tgrs.2006.873853 (2006).

35 Wegmuller, U., Werner, C. & ESA. in *Third Ers Symposium on Space at the Service of Our Environment, Vols. Ii & Iii* Vol. 414 *ESA Special Publications* 1687-1692 (1997).

36 Michel, R., Avouac, J. P. & Taboury, J. Measuring ground displacements from SAR amplitude images: application to the Landers earthquake. *Geophysical Research Letters* **26**, 875-878 (1999).

37 Wang, T., Jonsson, S. & Hanssen, R. F. Improved SAR Image Coregistration Using Pixel-Offset Series. *IEEE Geoscience and Remote Sensing Letters* **11**, 1465-1469, doi:10.1109/lgrs.2013.2295429 (2014).

38 Jonsson, S., Zebker, H., Segall, P. & Amelung, F. Fault slip distribution of the 1999 M-w 7.1 Hector Mine, California, earthquake, estimated from satellite radar and GPS measurements. *Bulletin Of The Seismological Society Of America* **92**, 1377-1389 (2002).

39 Bamler, R. & Eineder, M. Accuracy of differential shift estimation by correlation and split-bandwidth interferometry for wideband and Delta-k SAR systems. *IEEE Geoscience and Remote Sensing Letters* **2**, 151-155, doi:10.1109/lgrs.2004.843203 (2005).

40 Tinti, E., Bizzarri, A. & Cocco, M. Modeling the dynamic rupture propagation on heterogeneous faults with rate- and state-dependent friction. *Annals of Geophysics* **48**, 327-345 (2005).

41 Mahesh, P. *et al.* One-Dimensional Reference Velocity Model and Precise Locations of Earthquake Hypocenters in the Kumaon-Garhwal Himalaya. *B Seismol Soc Am* **103**, 328-339 (2013).

Correspondence and requests for materials should be addressed to Jean-Philippe Avouac (avouac@gps.caltech.edu)

Acknowledgements: Sentinel-1A data are provided by the European Space Agency. TW thank J. Kim from SMU for helps in processing the SAR data. We thank three anonymous reviewers for their constructive comments and thoughtful suggestions, as well as the editor Amy Whitchurch. We also thank Roland Burgmann for comments on an earlier version of this study,

Authors contribution: JPhA coordinated the research and wrote the article. LM and JPA carried out the backprojection. SW carried out the finite-source modeling. TW carried out the SAR offset measurements. All authors contributed to the interpretation and writing of the article.

The authors declare no competing financial interests.

METHODS

We describe here the methods used in this study. The corresponding codes are not available on-line as these are not user-friendly codes with manuals, but they can be provided upon requests sent to the authors. The waveform data are available from the Incorporated Research Institutions for Seismology web site (http://www.iris.edu/hq/).

Back projection of high frequency teleseismic seismic waveforms

The coseismic rupture process of 2015 Mw 7.8 Gorkha earthquake is well imaged by the back-projection (BP) approach, which provides a high frequency view of the rupture process. In contrast to classic source inversions based on waveform fitting, the approach does not require the detailed knowledge of the Green's function and relies solely on the timing information of coherent seismograms. The BP approach is therefore less affected by the uncertainty of seismic velocity structures or the assumptions of fault geometry and rupture kinematics. The BP analysis is typically performed on coherent seismograms recorded at teleseismic distances. Here, we use the seismograms recorded by the Australian seismic network (AU), composed of 54 broadband stations evenly distributed across the continental Australia with epicentral distances between 60° and 95° (Fig. S1). The data of the AU network are available from the IRIS data center (http://www.iris.edu). We band pass the AU seismograms between 2 s and 0.5 s, the highest band with relatively high waveform coherency (Fig. S2). We aligned the initial P-wave arrivals of the filtered waveforms with a multi-channel cross-correlation technique[30]. The first arrival is assumed to come from the USGS hypocenter location (84.71 °E, 28.15 °N). The location of the later HF sources are determined based on the differential travel time relative to the hypocenter. Since differential travel time is not sensitive to relatively small source depth changes along the shallow dipping MHT, we back-projected the waveforms onto a horizontal fault plane at a depth of 15 km based on the IASP91 velocity model. We adopted the Multitaper-MUSIC array processing technique[31] which resolves more closely spaced sources and are less sensitive to aliasing, yielding a sharper image of the rupture process than the standard beamforming approach[32]. We also applied a "reference window" strategy[33], which eliminates the "swimming" artifacts, a systematic apparent drift of the HF energy towards the station arrays.

SAR Data and processing

We used two pairs (descending Path 19 and ascending Path 85) of Sentinel-1A Synthetic Aperture Radar (SAR) images from the European Space Agency to map the surface deformation caused by the earthquake. The radar images were acquired in the Terrain Observation by Progressive Scan (TOPS) mode, which is designed for carrying out routine, SAR-based observations[34]. We aligned the post-seismic image (acquired on April 29th and May 3rd) along with the pre-seismic image (acquired on April 17th and 9th) by using the GAMMA software[35], and then calculated cross-correlation between uniformly distributed non-overlapping 64-by-64 sub-images on the co-registered radar amplitude images. The peak location in the obtained cross-correlation surface indicates the offset between the two sub-images in azimuth (satellite traveling direction) and in range (radar line-of-sight direction, LOS)[36,37].

Offsets between the SAR image pair are attributed to the ground displacement as well as to imaging geometry differences and topography. We therefore calculated the geometric offsets from the orbital information and the Shuttle Radar Topography Mission Digital Elevation Model (SRTM DEM)[37]. After the geometric correction, a low-frequency trend still exists in the offsets field, probably due to the inaccurate orbital information. We removed this component by fitting a polynomial surface from the offsets located in the far field. We used an initial slip model to generate two synthetic surface displacements in the radar LOS and azimuth directions. The derived range offsets measure ground displacement in the radar LOS directions that are from 32 to 46 degrees from the vertical with a component towards the west and east, while the azimuth offsets measures along-track components, which is in about SSW (191°eastward from North) and NNW (11°westward from North) for the descending and ascending data, respectively. For each downsampled data point, we calculated the line-of-sight vector based on its geo-location and the satellite orbital information. We used the predicted displacements to generate two quadtree sub-sampling grids[38], on which we extracted median values from offsets within each grid, resulting in 263 and 715 data points in azimuth and range from the descending track P19, and 499 and 786 data points from the ascending track P85, in azimuth and range, respectively (Figure S3).

The accuracy of SAR image offsets depends on the cross-correlation peak and can reach around 1/10 - 1/20 of the pixel spacing[39]. For the Sentinel-1A TOPS image, the azimuth and range pixel spacing are 14 m and 2.3 m respectively, as a consequence, azimuth offsets are only useful when the north-south component of the horizontal deformation is large, which is the case for the Gorkha earthquake. Range offsets measure the surface deformation in the same direction as interferometry, which can be formed from the same SAR image pair. However the phase information is seriously decorrelated in the Himalaya mountainous areas. In addition, the high deformation gradient surrounding the peak deforming area may result in aliasing phase values. Both factors can cause un-reliable phase unwrapping results, we therefore decide to use image offsets data for our model inversion.

Finite source modeling and inversion procedure

We downloaded GSN broadband data from the IRIS DMC. We analyzed 40 teleseismic P and 37 SH waveforms selected based upon data quality and azimuthal distribution. Waveforms are first converted to displacement by removing the instrument response at the frequency range lower than 1Hz. The geodetic data were obtained by cross-correlation of sentinel-1 SAR data, both for ascending and descending images (see previous section for more details).

We approximate the fault geometry with a planar fault segment with strike of 293° and dip of 7° (GCMT), each discretized in 8×8 km^2 subfaults. The model assumes that the rupture consists of propagating rupture front with slip accruing in the wake of the passage of the rupture front. The slip history at each grid point (j,k) on the fault is represented by $D \times \dot{S}_{jk}(t)$, where $\dot{S}_{jk}(t)$ is the slip-rate function which specifies how a point on the fault slips in time, and D is the cumulative (or 'static') slip. The rise-time function is represented by a cosine function parameterized by the duration of slip, the so-called rise-time. Because the seismograms are bandpass-filtered, this rather smooth slip-rate function is adapted although a more abrupt slip-rate function would probably be more realistic[40]. For each subfault, we solve for the slip amplitude and rake, rise time and rupture velocity. The Green's functions are generated assuming a 1-D model derived a local seismic network[41] (Table S1).

The determination of a finite fault slip model is an underdetermined problem due to the large number of unknowns and numerous trade-off among model parameters, such as rise time and rupture velocity. In the present case the trade-offs are significantly reduced if coseismic geodetic observations are available and inverted jointly with the seismological data. Even so, the determination of a finite fault source remains generally underdetermined if the fault discretization is too fine. One way to regularize the inversion is setting some constraints on the roughness of the slip distribution which is the approach adopted here.

We define the best fit model as having the lowest objective function, given as:

*Misfit= Ewf+ WI *EI +WS *S + Ww*M*,

where *Ewf* is the waveform misfit, *EI* is the geodetic misfit, *S* is a normalized, second derivative of slip between adjacent patches (a so-called Laplacian smoothing). *M* is a normalized seismic moment, and *WI*, *WS* and *Ww* are the relative weighting applied to the geodic misfit, smoothing, and moment, respectively. The least squares misfits are calculated for the teleseismic and geodetic data. Here we test different values of *WI*, and we found that by setting the weight for the geodetic misfits twice as large as for the waveform misfits did not significantly degrade the fits to the teleseismic or geodetic data between the individual and joint inversions given the normalizations schemes. The static Green's functions at free surface are calculated by using the same 1D velocity model (Table S1) as used in teleseismic body-wave calculation. The fit to the P-waves is given twice as much weight as that to the SH-waves. There are mainly two reasons for this: 1. It is much easier to pick P-wave first arrivals than SH-wave, due to larger noise in the SH-waves; 2. The SH-waves are usually more sensitive to the 3D velocity structure. Thus in general, the SH-wave fits are not as good as P-waves, in particular for thrust events. Here the P-waves and geodetic data are the most robust and clean data and thus provide the better constrains on the rupture process.

We use a simulated annealing algorithm[13] to find the best fitting model parameters for the joint inversions for coseismic slip. This nonlinear, iterative inversion algorithm is designed to avoid local minima by searching broadly through parameter space in initial steps, and then in later iterations to focus on regions that fit the data well.

We determined the best-fitting mean rupture velocity by imposing the rupture velocity to be constant. Figure S5 shows how the fit to waveforms varies for rupture velocities between 1 and 4km/s. The best fitting value is 3.0+/-0.5km/s. We next performed an inversion with variable rupture velocity (Figure S6).

Supplements to ‘Lower edge of locked Main Himalayan Thrust unzipped by the 2015 Gorkha earthquake’

Jean-Philippe Avouac, Lingsen Meng, Shengji Wei, Teng Wang, Jean-Paul Ampuero

Supplementary animation : ‘GorkhaEQ-kimematics.gif’ shows the time evolution of the seismic rupture during the Mw 7.8 Gorkha earthquake of April 25, 2015 derived from our seismological study. Each frame shows slip (background color shading) occurring within a 3 s window indicated by a grey band over the source time function in the inset. The high-frequency sources imaged by back-projection up to the snapshot time (dots, colored by their rupture time) are also plotted up to the frame time.

Table S1: 1D velocity model in the source region.

Vp(km/s)	Vs(km/s)	Density(g/cm^3)	Thickness (km)
5.50	3.20	2.53	4.0
5.85	3.40	2.64	12.0
6.00	3.50	2.69	4.00
6.45	3.70	2.83	6.50
6.65	3.85	2.90	10.00
7.20	4.15	3.07	5.00
7.50	4.20	3.17	14.00
7.90	4.30	3.30	15.00

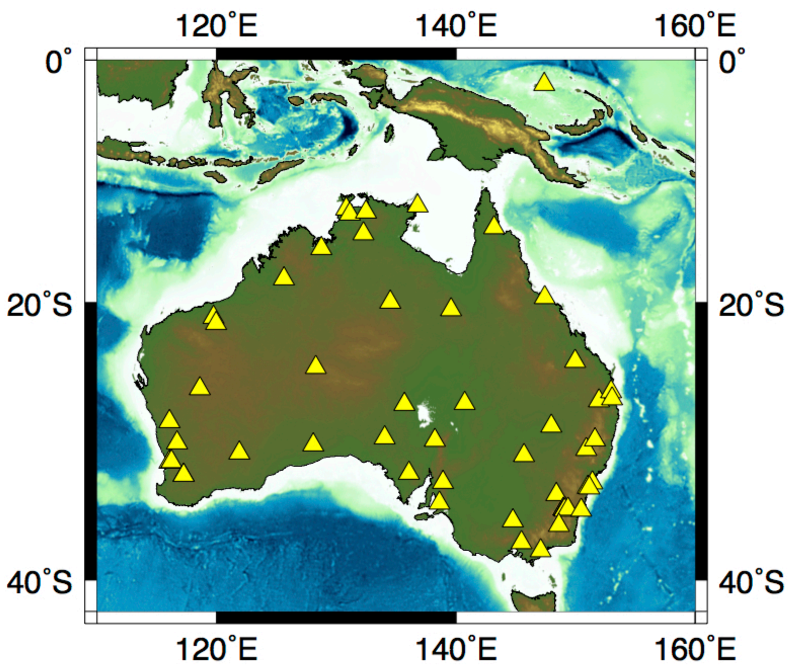

Figure S1: Station distribution of the Australian seismic network. Yellow triangles indicate the stations used in the high frequency back-projection analysis.

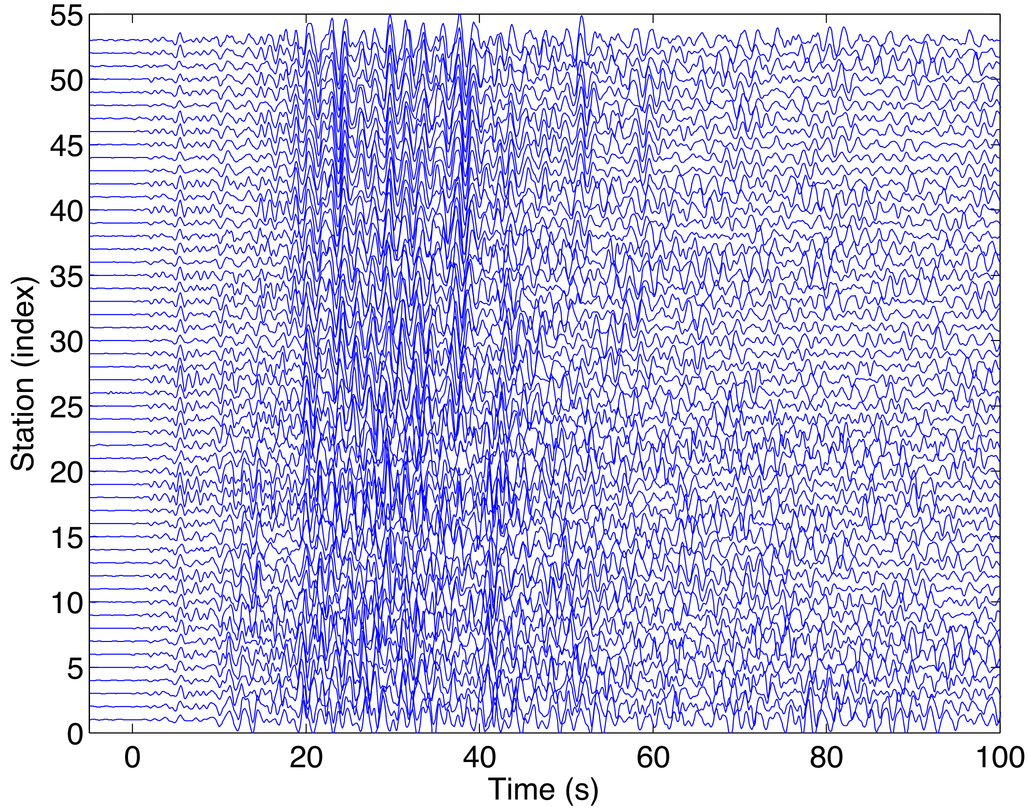

Figure S2: Seismograms (0.5 - 2 Hz) of the Gorkha earthquake recorded by the Australian seismic network. The direct P-wave arrival is aligned at time zero. The station index is ordered by epicentral distance.

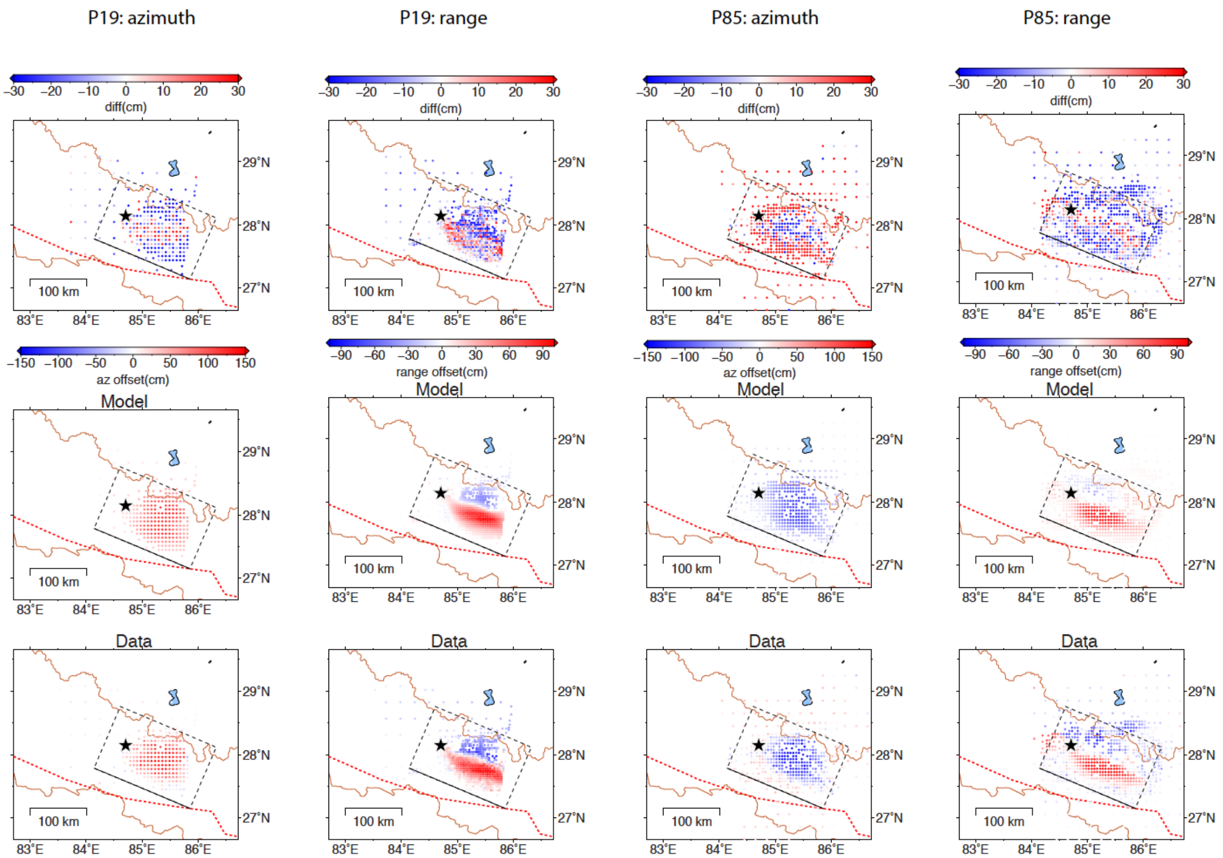

Figure S3: Comparison between the predicted and observed surface displacements derived from cross-correlation of descending (P19) and ascending (P85) images.

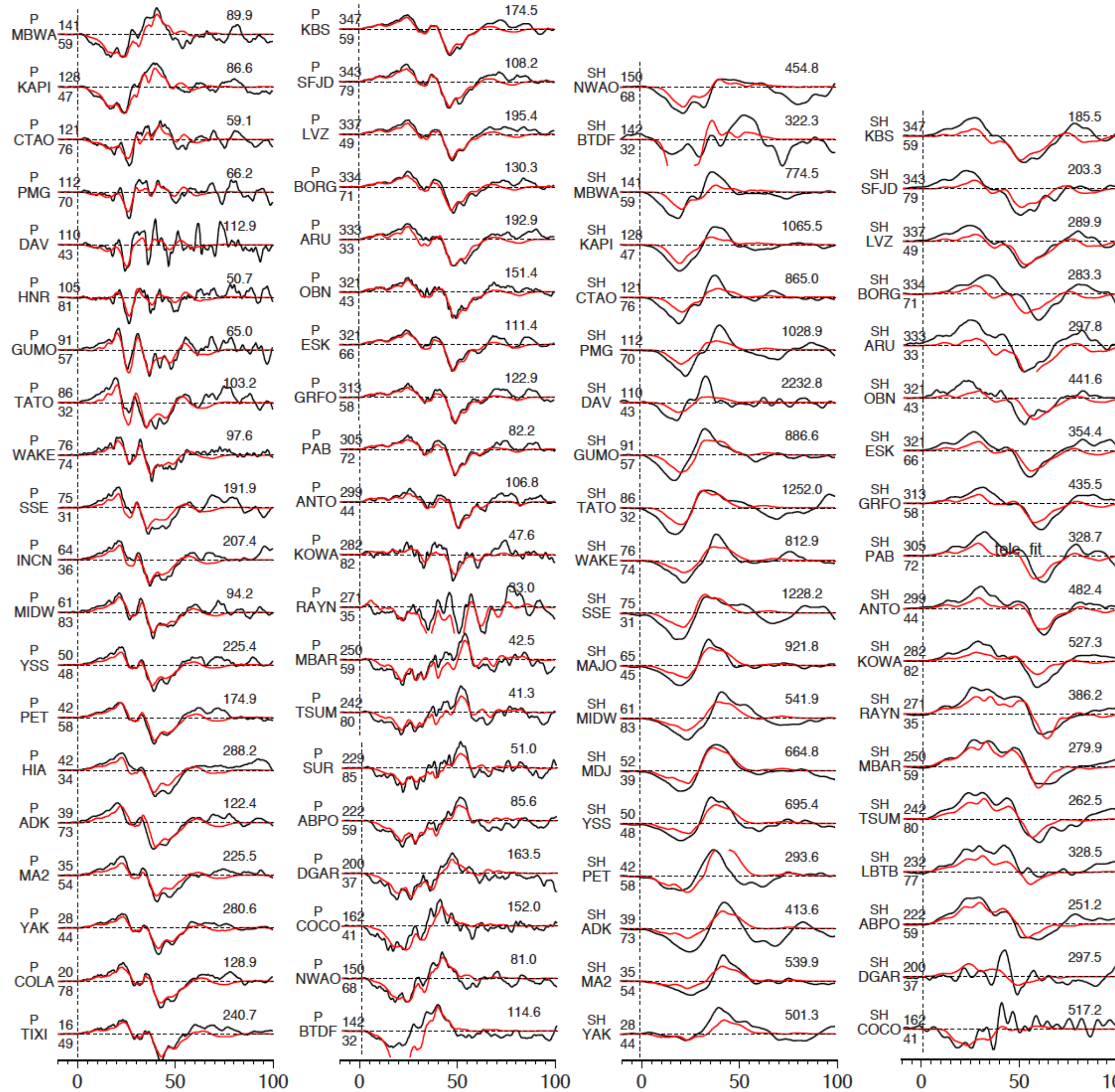

Figure S4 : Comparison between measured (black) and synthetic (red) teleseismic waveforms on the selected stations with P-waves shown on the left and SH-waves on the right (time in seconds). Stations names are shown on the left of each waveform comparison along with azimuth (upper) and epicenter distance (lower) in degree. Stations are arranged such that the azimuth increases from bottom to the top. Note that the SH-waves are much broader in the direction away from the rupture than that towards the rupture, as indicated by the red arrows.

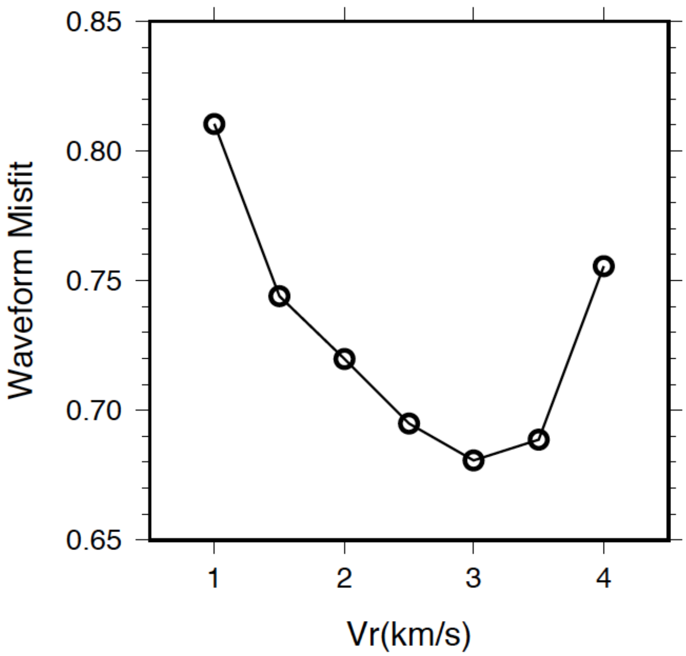

Figure S5: Misfit between observed and synthetic waveforms for models with imposed constant rupture velocity.

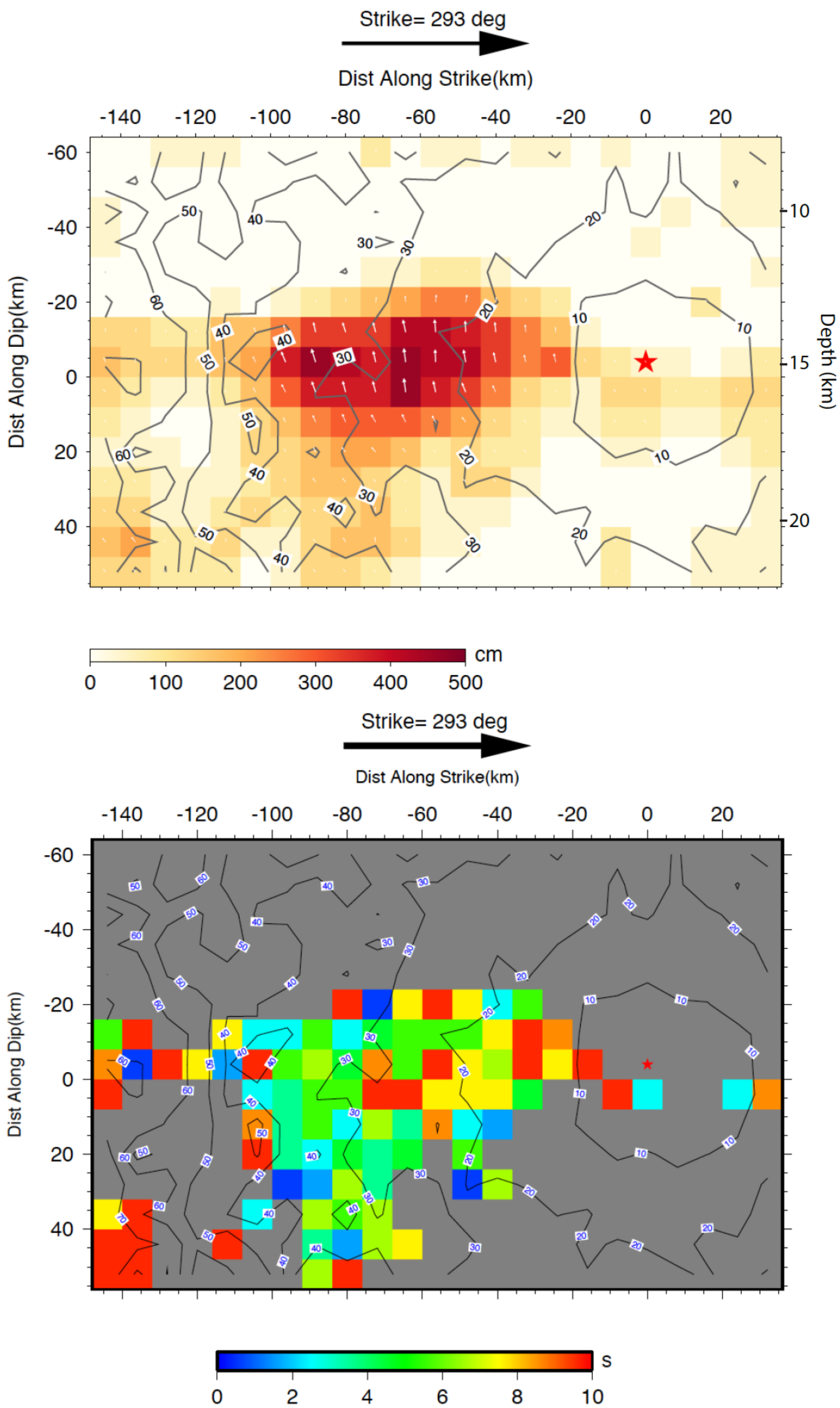

Figure S6: Top: Slip distribution in depth view, arrows indicate the rake angle and the slip amplitude is color coded. Rupture times are indicated by the contours. Bottom: Rise time distribution in depth view, only shows the slip patches with slip amplitude larger than 1 m.